IEEE Access
Multidisciplinary | Rapid Review | Open Access Journal

Received August 18, 2018, accepted October 5, 2018, date of publication October 11, 2018, date of current version November 8, 2018.

Digital Object Identifier 10.1109/ACCESS.2018.2875413

Modeling and Decoupled Control of Inductive Power Transfer to Implement Constant Current/Voltage Charging and ZVS Operating for Electric Vehicles

CHENG CHEN[1], (Student Member, IEEE), HONG ZHOU[1], (Member, IEEE), QIJUN DENG[1,2], WENSHAN HU[1,2], (Member, IEEE), YANJUAN YU[3], XIAOQING LU[1], AND JINGANG LAI[4], (Member, IEEE)

[1]School of Power and Mechanical Engineering, Wuhan University, Wuhan 430072, China
[2]Wuhan University Shenzhen Research Institute, Shenzhen 518057, China
[3]School of Electrical Engineering, Wuhan University, Wuhan 430072, China
[4]School of Engineering, RMIT University, Melbourne, VIC 3001, Australia

Corresponding authors: Qijun Deng (dqj@whu.edu.cn) and Wenshan Hu (wenshan.hu@whu.edu.cn)

This work was supported in part by the National Natural Science Foundation of China under Grant 51677139 and Grant 61873195 and in part by the Basic Research Project of Shenzhen Science and Technology Commission under Grant JCYJ20170818112806 74.

ABSTRACT To prevent the degradation of battery life and reduce switching loss in inductive power transfer (IPT) systems for electric vehicles (EVs), it is vital to realize constant current/voltage (CC/CV) charging and zero-voltage-switching (ZVS) operation. However, due to the existence of couplings between the charging and ZVS operating control loops, the controllers are neither optimal nor robust. In this paper, a model-based decoupled control method is proposed to improve the performance of the charging and ZVS operating controllers. Since the operating point of the CC and CV modes are different, two dynamic models for the corresponding charging modes are built and linearized. Besides, the couplings between the charging and ZVS operating control loops are analyzed, and in turn, decoupled by designing compensators. To optimize the system performance, we chose PI controllers, and their parameters are obtained by calculating the settling time and overshoot of the close-loop dominant poles according to the control performance requirements. In the experiment, a 500-W series–series IPT system prototype is built and tested to verify the improvement of the control performance. Compared with the coupled control method and the traditional closed-loop control feedback method, the recorded response curves and transient waveforms demonstrate that the proposed decoupled control method brings a better performance to the system.

INDEX TERMS Inductive charging system, modeling, zero voltage switching; decoupled control;

I. INTRODUCTION

Inductive power transfer (IPT), or wireless power transfer (WPT) is a highly-regarded technology that makes the energy transfer process safer, more reliable, and more user-friendly [1], [2]. For the application of the wireless charging systems (WCS) for electric vehicles (EVs), since the power can be directly picked up from the parking spaces or roads, the WCS are considered as one of the practicable methods to increase the competitiveness of EVs for thermal vehicles [4]–[7].

In order to reduce the switching loss and to prevent the degradation of the battery's lifespan, the WCS is usually expected not only to provide constant current/voltage (CC/CV) charging [6], [7] but also to realize zero-voltage-switching (ZVS) operation [7], [8], [10]. However, there is a common challenge for the WCS, that is, the CC/CV charging and ZVS operating are easily fluctuated by the changes in the battery resistance during the charging process [5]–[7], which leads to neither optimal nor robust charge process for EVs. Therefore, numerous controllers or strategies in previous works are designed to mitigate the perturbance.

The proportional–integral (PI) control method is adopted in [7] and [10]–[14], while phase-locked-loop (PLL) [8], [10], proportional–differential (PD) controller [13], algorithms [14], [16] and sliding-mode controller [18], [19] are

2169-3536 © 2018 IEEE. Translations and content mining are permitted for academic research only.
Personal use is also permitted, but republication/redistribution requires IEEE permission.
See http://www.ieee.org/publications_standards/publications/rights/index.html for more information.

developed to regulate the charging current, voltage and ZVS angle. In these studies, the duty cycle [7], [8] and the operating frequency [7]–[10] of the inverter are usually selected as the controlled quantities to form a charging and a ZVS operation control-loops, respectively. Although a ZVS angle [7], [10] can be accurately calculated by considering the whole time delays synthetically, the parameters of the PI and PLL controllers are not optimized, resulting in a volatile control performance of the output current or voltage. Considering that the primary current and the secondary output voltage are easily adjusted by the power source and DC-DC converters [11]–[18], the PI or PD controllers [11]–[14], customized algorithms [14], [16] and sliding-mode controller [18] are used to controlling the outputs of the pulse width modulation (PWM) regulators or active rectifiers. To tune the parameters of the controllers, an empirical Ziegler–Nichols (ZN) method is adopted in [11] and [12]. Furthermore, the above researchers mainly focus on the steady state of the system rather than the dynamic performance like overshoot and settling time. Thus, the dynamic performance of the control-loops is neither analyzed nor considered in the design of the controllers [14]–[18].

It is well known that the dynamic performance of the model is essential for designing controllers because the steady-state model is incapable of providing an accurate insight into the transient behaviours of the system and evaluating the maximum stresses during startup and shutdown processes [20]. Thus, in many industrial applications, the settling time and overshoot of the controllers should be optimized according to the performance requirements. Moreover, because the WCS with the charging and ZVS operation controllers are multivariable systems, the couplings between the model inputs should be clarified. Therefore, there is a need for dynamic modeling, which can be used to analyze the dynamic performance and couplings during the design process of the controllers.

In addition, it is necessary to take into account the fact that the operating point of the system changes as the charging mode switching while designing controllers for both CC and CV modes. To deal with this problem, two closed control-loops with PI controllers for CC/CV modes based on the first harmonic equivalent models are proposed in [21] and [22] to regulate the charging process and to maintain the ZVS operation. The output gain and phase of each charging mode are analyzed in the frequency domain. Unfortunately, although the control performance can be improved, these models are static and, as such, they are inconvenient to analyze the dynamics and couplings of the system during the design of controllers. Therefore, different modeling methods are proposed in [20] and [23]–[32] to find an appropriate dynamic model. For example, a model based on the Laplace phasor transform theory [23], [24] is adopted to analyze the dynamics of the circuits. The *LCL* circuit [20], [25], *LCC* circuit [26], converters [27] and S-S compensation circuits [28]–[31] of the IPT and WPT system are modeled using generalized state space averaging (GSSA) method. Typically, based on [20] and [29], authors in [31] propose two transfer function models for control-to-output corresponding to the CC and CV modes. Compared to [21] and [22], these models provide good insights on the envelope of charging current and voltage and give a numerical analysis on the dynamic performance such as the magnitude-phase characteristics of the CC and CV control-loops. However, it is difficult to describe the state of the ZVS operation by the proposed state variables, resulting in an additional current stress optimization controller on the primary side to maintain the ZVS operating. In [32], a Coupled-Mode theory [34] based model, covering the ZVS angle, charging current and voltage, is proposed for analyzing and controlling the output voltage. Since the state variables of the dynamic differential equations of the circuit can be replaced by the phase angle and amplitude of the coupled modes, it is more suitable to design a controller to regulate the charging and ZVS operation of this model. Also, based on this modeling method, the couplings between the inputs of the multivariable WCS models can also be decoupled by evaluating the static gain of each control loop.

The main purpose of this paper is to improve the performance of the WCS throughout the whole charging period by proposing a decoupled control method. To overcome the perturbance of the system operating point, two dynamic models for CC and CV modes are constructed and linearized, to analyze the dynamic performance of the system. Moreover, the couplings between the inputs of the charging and ZVS operating controllers are quantified using static gains. By introducing decoupled compensators and PI controllers, the decoupled control method for IPT system is proposed and implemented to regulate the charging process and ZVS operation. Compared to the coupled control methods and the traditional closed-loop control feedback methods, the recorded response curves and transient waveforms demonstrate that the proposed decoupled control method brings better performance. Differentiating from the existing works, the contributions of this paper are as follows:

(1) Considering that the dynamic models are different in CC and CV modes, a fourth-order and a fifth-order models are developed, respectively, to prevent the weakening of the performance of the system.
(2) The static gains are used to evaluate the couplings between the inputs of the charging and ZVS operating controllers. By designing decoupled compensators, the multivariable CC and CV models are equivalent to two single variable models and, in turn, they become easier to design controllers to regulate the dynamical behaviours of the decoupled systems.
(3) To optimize the system performance, we chose PI controllers, and their parameters are obtained by calculating the settling time and overshoot of the close-loop dominant poles according to the requirements of the control performance, which is especially useful when the control system is required to be designed tightly.

The rest of this paper is organized as follows: Section II analyses the input impedance, ZVS angle and outputs of the WCS and proposes a decoupled control strategy. Section III focuses on the dynamic modeling and linearization of the CC and CV modes. To optimize control performance, a decoupled control method including compensators and PI controllers are proposed in section IV. A physical prototype is set up in Section V, and the recorded response curves and transient waveforms demonstrate that the proposed decoupled control method brings better performance to the system.

II. ANALYSIS OF THE SYSTEM STRUCTURE

A. STRUCTURE OF THE BASIC S-S WCS

A common series–series (S-S) compensated topology for WCS, as shown in Fig. 1, is composed of a controllable DC source, a high-frequency half-bridge inverter, a symmetrical S-S resonant network, a full-bridge rectifier and a battery equivalent series resistance (ESR). The DC source converts a three-phase AC voltage into a controllable DC voltage source V_{I} by regulating the driver of the converter. Then, the resonant network and the full-bridge rectifier are activated by the high-frequency half-bridge inverter to charge the battery wirelessly. Each resonant tank includes a series capacitance, an inductance and its ESR, respectively. The symbol i_{p} and i_{s} are the resonance current through the coils; v_{p} and v_{s} are the voltage across the capacitors. M is the mutual inductance between two coils.

To realize the charging control and the ZVS operation control, the controllable V_{I} and the operation frequency f_{o} are adjusted by the proposed decoupled control method, as shown in Fig.1. In detail, by detecting the zero-crossing of i_{p} and the rising edge of the gate-driving signal of the inverter, the phase difference between i_{s} and v_{ab} can be obtained to predict the state of the ZVS operation In order to implement the CC and CV charging mode, the output current and voltage are detected to form a current and a voltage feedback control-loops, respectively, by using a common wireless communication module. The parameters of the PI controllers in CC and CV modes are optimized based on the respective dynamic models and performances to overcome the perturbance caused by the change of the operating point. In addition, the control performance of the controllers is improved because the couplings between the ZVS control-loop and the charging control-loop is cancelled by the decoupled compensators.

B. ANALYSIS OF THE CIRCUIT

Assuming that:

(1) The resonant currents, i_1 and i_2, are pure sinusoidal.
(2) The filter capacitance of the full-bridge rectifier is big enough.

The fundamental components of the inverter output voltages v_{ab} and the ESR R_{cd} of the full-bridge rectifier can be replaced by

$$v_{\mathrm{ab}} = \left(2V_{\mathrm{I}} \cos \omega_{\mathrm{s}} t\right) / \pi, \tag{1}$$

$$R_{\mathrm{cd}} = 8R_{\mathrm{b}} / \pi^2, \tag{2}$$

where ω_{s} and R_{b} are the angular switching frequency of the bridge inverter and the ESR of the battery, respectively. Therefore, the main circuit of the WCS can be equivalent to a fundamental harmonic equivalent circuit, as depicted in Fig. 1. The charging voltage and current of the battery are labelled as V_{o} and I_{o}, respectively. The input impedance Z_{in} of the equivalent circuit can be expressed per:

$$Z_{\mathrm{in}} = Z_{\mathrm{p}} + (\omega_{\mathrm{s}} M)^2 / (Z_{\mathrm{s}} + R_{\mathrm{cd}}), \tag{3}$$

where Z_{p} and Z_{s} stand for the primary and secondary resonant network impedance, respectively. According to [7], the ZVS angle φ_{zvs} can be depicted as

$$\varphi_{\mathrm{zvs}} = \Delta\varphi - \varphi_d = \arctan\left(\frac{\mathrm{Im}\left[Z_{\mathrm{in}}\right]}{\mathrm{Re}\left[Z_{\mathrm{in}}\right]}\right) - \frac{(1 - D_{\mathrm{inv}})\,\pi}{2}, \tag{4}$$

where $\Delta\varphi$ is the phase angle of the input impedance Z_{in}, φ_{d} is the phase angle of the dead-time of the inverter, and D_{inv} denotes the duty cycle of the square wave drive signal of the inverter.

According to the equivalent circuit, one obtains that the equivalent input voltage source v_{cd} of the full-bridge rectifier [35] is as follow:

$$\begin{aligned} v_{\mathrm{cd}} &= j\omega_s M \frac{v_{\mathrm{ab}}}{Z_{\mathrm{in}}} + i_{\mathrm{s}} Z_{\mathrm{s}} \\ &= \mathrm{sign}\left(i_{\mathrm{s}}\right) \cdot V_{\mathrm{o}}. \end{aligned} \tag{5}$$

It can be observed that the magnitude of v_{cd} is equal to the charging voltage V_{o}, and the direction is decided by the sign of i_{s}. In addition, the equivalent DC current source I_{F} of the $R_{\mathrm{battery}} - C_{\mathrm{f}}$ circuit input is a function of the rectifier input AC current i_{s} [35], which can be represented by the following expression:

$$I_{\mathrm{o}} = I_{\mathrm{F}} - i_{\mathrm{cf}} = |i_{\mathrm{s}}| - i_{\mathrm{cf}}. \tag{6}$$

Considering (1)-(6), one can draw a conclusion that the charging voltage V_{o} and the current I_{o} can be controlled by adjusting V_{I}. Meanwhile, the ZVS angle φ_{zvs} can remain a constant by regulating the angular switching frequency ω_{o}. Notably, due to the couplings of the multivariable systems, the charging voltage and current are fluctuated with ω_{o} at this time. Therefore, the decoupled control strategy for the battery charging and system ZVS operation is proposed in Fig. 2. The parameters of the PI controllers in CC and CV modes are optimized based on the respective dynamic models and performances to overcome the perturbance caused by the change of the operating point. Besides, the compensators are designed based on the static gains and are utilized to neutralize the couplings of the system.

III. DYNAMIC MODELING OF THE SYSTEM

In this section, the dynamic models of the CC and CV charging modes covering the states of the ZVS angle, charging current and charging voltage are developed and linearized.

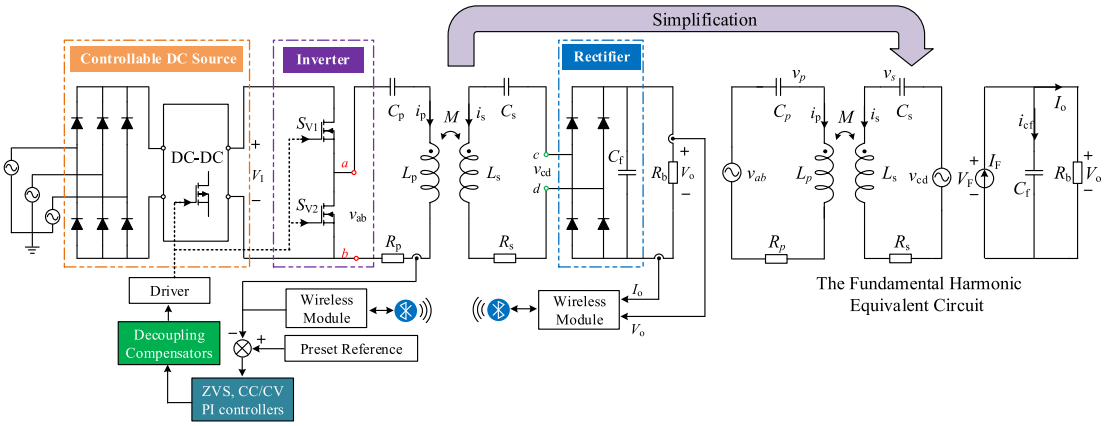

FIGURE 1. Circuit diagram of the S-S compensated wireless charging system.

A. THE DYNAMIC DIFFERENTIAL EQUATIONS

According to the fundamental harmonic equivalent circuit of the system in Fig. 1, the electric behaviours of the IPT system can be described by the following fourth-order dynamic differential equations:

$$\begin{cases} v_{ab} = i_p R_p + v_p + L_p \dfrac{di_p(t)}{dt} + M \dfrac{di_s(t)}{dt} \\ i_p = C_p \dfrac{dv_p(t)}{dt} \\ M \dfrac{di_p(t)}{dt} = v_{cd} - v_s - i_s R_s - L_s \dfrac{di_s(t)}{dt} \\ i_s = C_s \dfrac{dv_s(t)}{dt} \end{cases} \tag{7}$$

Similar to the models in [23]–[30], these equations cannot be used to analyze the dynamic performance of the ZVS operation directly. Therefore, it is necessary to establish the relationship between state variables in (7) and the phase angle of the coupled network. According to the suggestion in [32] and [33], the dynamic characteristics of the system can also be described by the Coupled-Mode theory [34]. To acquire a dynamic model covering the ZVS angle, charging current and voltage, the state variables of the coupled circuit in (7) are represented by the amplitude $a_{p,s}$ and phase angle $\theta_{p,s}$ of the coupled modes [32], [33] as

$$\begin{cases} i_{p,s} = \sqrt{2/L_{p,s}} \cdot a_{p,s} \cos\left(\omega_s t + \theta_{p,s}\right) \\ v_{p,s} = \sqrt{2/C_{p,s}} \cdot a_{p,s} \sin\left(\omega_s t + \theta_{p,s}\right). \end{cases} \tag{8}$$

Thus, one obtains a nonlinear time-invariant averaged model of the WCS given as following:

$$\begin{cases} \dot{x} = f(x) + g(x)\, u \\ y = h(x), \end{cases} \tag{9}$$

where $x = [a_p, \theta_p, a_s, \theta_s]^T$ and $u = [f_o, V_I]^T$ are the state vector and inputs of the model, respectively; $h_{zvs}(x)$ is the output of the ZVS angle φ_{zvs}; $h_{cc}(x)$ and $h_{cv}(x)$ are the outputs of the charging current and voltage, respectively, which will be detailed subsequently in the next subsections; $f(x)$ and $g(x)$ are smooth nonlinear functions given by

$$f(x) = \begin{pmatrix} K_1\left(-K_3 S_1 x_3 + K_5 M S_2 x_3 - M K_6 L_s x_1\right) \\ \dfrac{\omega_p}{2} - \dfrac{K_1}{a_p}\left(K_3 S_2 x_3 + K_5 M S_1 x_3 - K_7 x_1\right) \\ K_2\left(K_4 S_1 x_1 + K_6 S_2 x_1 - K_5 L_p x_3\right) \\ \dfrac{\omega_s}{2} - \dfrac{K_2}{a_s}\left(K_4 S_2 x_1 - K_6 S_1 x_1 - K_8 x_3\right) \end{pmatrix}, \tag{10}$$

$$g_{V_I}(x) = \frac{1}{\pi}\begin{pmatrix} K_1 L_s \cos x_2 \\ -\dfrac{K_1 L_s}{x_1} \sin x_2 \\ -K_2 M \cos x_4 \\ \dfrac{K_2 M}{x_3} \sin x_4 \end{pmatrix}, \quad g_{\omega_o}(x) = \begin{pmatrix} 0 \\ -1 \\ 0 \\ -1 \end{pmatrix}, \tag{11}$$

respectively, where S_1, S_2 and the variables K_1-K_8 are listed in the Appendix. For the control of the ZVS operating, the angle φ_{zvs} should be a constant no matter the system is in the CC or CV charging mode, so the output of ZVS angle can be defined as

$$h_{ZVS}(x) = -\frac{180}{\pi}\left(x_2 + \frac{(1 - D_{inv})\,\pi}{2}\right). \tag{12}$$

Since the operating point of the system will change as the charging mode switches, the dynamic models of the CC and CV charging modes need to be derived, respectively.

B. CC AND CV NONLINEAR DYNAMIC MODEL

Taking the average values during a switching period, the equation (6) yields the DC component of the charging current [35]:

$$I_o = \frac{1}{2\pi}\int_0^{2\pi} i_s d(\omega_o t) = \frac{2}{\pi} I_{sm}, \tag{13}$$

which is proportional to the amplitude I_{sm} of the secondary current. The output of the charging current in the CC mode with the state vector $x_{CC} = [a_{ccp}, \theta_{ccp}, a_{ccs}, \theta_{ccs}]^T$ can be

defined as

$$h_{\mathrm{CC}}\left(x_{\mathrm{CC}}\right)=\frac{2}{\pi}\sqrt{\frac{2}{L_s}}a_{\mathrm{ccs}}. \tag{14}$$

Thus, the nonlinear dynamic model of the CC mode can be derived by combining (9)-(12) and (14). Moreover, the energy storage element C_{f} in Fig. 1 can be described by an additional differential equation

$$C_{\mathrm{f}}\frac{dV_{\mathrm{o}}}{dt}=I_{\mathrm{F}}-\frac{V_{\mathrm{o}}}{R_{\mathrm{b}}}. \tag{15}$$

By substituting (14) into (7), a fifth-order nonlinear time-invariant averaged model of the CV mode is obtained as follow:

$$\begin{cases}\dot{x}=f\left(x\right)+g\left(x\right)u\\ \dfrac{dx_5}{dt}=\dfrac{1}{C_{\mathrm{f}}}\left(\dfrac{2}{\pi}\sqrt{\dfrac{2}{L_{\mathrm{s}}}}x_3-\dfrac{x_5}{R_{\mathrm{b}}}\right),\end{cases} \tag{16}$$

where the state vector of the CV mode is $x_{\mathrm{CV}}=[a_{\mathrm{cvp}},\theta_{\mathrm{cvp}},a_{\mathrm{cvs}},\theta_{\mathrm{cvs}},V_{\mathrm{o}}]^{\mathrm{T}}$, and the output of the charging voltage in the CV model with the above state vector can be defined as

$$h_{\mathrm{CV}}\left(x_{\mathrm{CV}}\right)=V_o. \tag{17}$$

C. MODEL LINEARIZATION

The nonlinear time-invariant averaged models of the CC and CV modes represent the envelope of the charging current, voltage and ZVS angle of the WCS. In other words, these models contain both the steady-state operating points and the small-signal models. Thus, each state variable in (9)-(12) and (14)-(16) can be written as the sum of the steady-state value and a small perturbation around it [29], [36]

$$x=x_{\mathrm{o}}+\Delta x. \tag{18}$$

Therefore, the nonlinear models can be linearized at the steady-state operation point and written in the state-space form as follows:

$$\begin{cases}\Delta\dot{x}=\mathbf{A}\cdot\Delta x+\mathbf{B}\cdot\Delta u\\ \Delta y=\mathbf{C}\cdot\Delta x,\end{cases} \tag{19}$$

where **A**, **B** and **C** are the partial derivative matrices of (10)-(12) and (14)-(17). To obtain the linearized small-signal models, the steady-state operating point should be calculated by setting the derivative terms in (9) and (16) to zero.

IV. SIMULATION ANALYSIS AND DESIGN OF THE DECOUPLED CONTROLLERS

In this paper, the reference constant charging current and voltage are set as 10 A and 50 V, respectively. Considering the analysis of the total loss [7] and the minimum phase angle [35] of the system, the reference ZVS angle is selected to be 20°. Since the battery resistance changes from 2.5 Ω to 5 Ω in the CC mode, and from 5 Ω to 15 Ω in the CC mode [5], the range of the load resistance in the CC and CV dynamic models are selected as 3.5-10 Ω. In order to achieve the expected charging curve and maintain the ZVS angle at the reference angle of 20°, the initial DC input voltage and operating frequency of the WCS in the CC and CV modes are set to be: 55 V and 88.5 kHz, 66 V and 82 kHz, respectively. According to the main parameters of the system in Table 1, one can obtain the operating points for the CC and CV charging modes as

$$\begin{aligned}x_{\mathrm{CCo}}&=\begin{bmatrix}0.05 & -0.35 & 0.04 & -2.9\end{bmatrix}^{\mathrm{T}}\\ x_{\mathrm{CVo}}&=\begin{bmatrix}0.07 & -0.35 & 0.03 & -2.13 & 50\end{bmatrix}^{\mathrm{T}}.\end{aligned} \tag{20}$$

By substituting (20) and Table 1 into the CC and CV nonlinear models, the partial derivative matrixes for the linearized small-signal state-space models are obtained:

$$\mathbf{A}_{\mathrm{CC}}=\begin{bmatrix}-7856 & 2332 & -4.1e4 & 1568\\ -9e5 & -8025 & 7.5e5 & -3.3e4\\ 3.2e4 & -2346 & -5.1e4 & 2210\\ 1.1e6 & 3.9e4 & -1.3e6 & -5e4\end{bmatrix}, \tag{21}$$

$$\mathbf{A}_{\mathrm{CV}}=\begin{bmatrix}7856 & 382 & -5.4e4 & 548 & -3.6\\ -7.4e4 & -8059 & 1.3e5 & -2.7e4 & -239\\ 5.4e4 & -939 & -7694 & 442 & -81\\ 4e5 & 1.2e5 & -4.2e5 & -1.3e5 & 0\\ 0 & 0 & 3.9e7 & 0 & -2.5e4\end{bmatrix}, \tag{22}$$

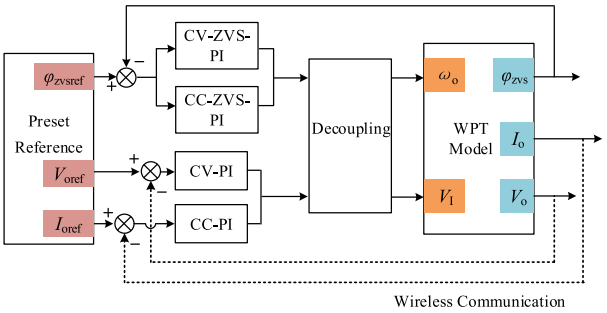

FIGURE 2. The decoupled control strategy for charging and ZVS operation of the system.

TABLE 1. Main parameters of the system.

Symbol	Quantity	Value
L_{p}	Resonant inductance on primary side	33.1 μH
C_{p}	Resonant capacitance on primary side	122.1 pF
R_{p}	The ESR at primary side	0.5 Ω
L_{s}	Resonant inductance on secondary side	34.3 μH
C_{s}	Resonant Capacitance on secondary side	121.9 pF
R_{s}	The ESR at secondary side	0.5 Ω
M	Mutual inductance between two coils	7.33 μH
C_{f}	Filtering capacitance	300 μF
D_{inv}	The duty cycle of drive signal for inverter	45 %
f_{o}	The range of the operating frequency	75-90 kHz
V_{I}	The range of the input DC voltage source	50-750 V

$$\mathbf{B}_{\mathrm{CC}} = \begin{bmatrix} 0 & 38.4 \\ -628.3 & 272.6 \\ 0 & 8.5 \\ -628.3 & -59.8 \end{bmatrix}, \quad \mathbf{B}_{\mathrm{CV}} = \begin{bmatrix} 0 & 38.4 \\ -628.3 & 195.6 \\ 0 & 4.7 \\ -628.3 & -231 \\ 0 & 0 \end{bmatrix}, \tag{23}$$

$$\mathbf{C}_{\mathrm{CC}} = \begin{bmatrix} 0 & -57.3 & 0 & 0 \\ 0 & 0 & 154.2 & 0 \end{bmatrix},$$
$$\mathbf{C}_{\mathrm{CV}} = \begin{bmatrix} 0 & -57.3 & 0 & 0 & 0 \\ 0 & 0 & 0 & 0 & 1 \end{bmatrix}. \tag{24}$$

Note that there is a limitation for these linearized models. When the load changes, the operating point of the system will deviate from the point at which the controller is designed, so the control performance of the controller will be weakened. More precise linearization of the system is interesting for future work.

A. DECOUPLED COMPENSATOR DESIGN

Since the linearized models developed above are multivariable models, the couplings between the inputs need to be clarified. Because if the coupling effect exists, when the inverter input DC voltage or operating frequency changes, the charging current, voltage and ZVS angle will all suffer from the perturbance. This mutual influence will weaken the control performance of the controllers, so it is necessary to evaluate and compensate this negative factor to improve the control performance.

For a MIMO system, the static gain p_{ij}, which represents the gain from the j-th input to the i-th output with the other inputs u_r $(r \neq j)$ remain unchanged, is defined as

$$p_{ij} = \left.\frac{\partial y_i}{\partial u_j}\right|_{u_r}. \tag{25}$$

The greater the value of p_{ij}, the more serious the coupling of the model will be. By using MATLAB, one can achieve the static gain matrices of the CC and CV linearized models (19)-(24) as follow:

$$p_{\mathrm{CC}} = \begin{bmatrix} 1.33 & 1.1e-5 \\ -0.07 & 0.158 \end{bmatrix}$$
$$p_{\mathrm{CV}} = \begin{bmatrix} 0.63 & 1.8e-4 \\ -0.23 & 0.71 \end{bmatrix}. \tag{26}$$

Obviously, the CC and CV linearized models are all semi-coupling because the static gains from u_2 to y_1 are small enough to be ignored. The unit step responses of the CC and CV linearized models without decoupled are plotted in Fig. 3. It can be seen that the input u_2 has little static deviation on the output y_1, while the output y_2 fluctuates with the step change of u_1. Notably, although the static deviation from DC input voltage to ZVS angle is small enough, the dynamic fluctuation in CV mode cannot be ignored. To eliminate these deviations and fluctuations, the feedforward compensators are adopted in this paper. The block diagram of the decoupled system is shown in Fig. 4(a). Based on the diagonal

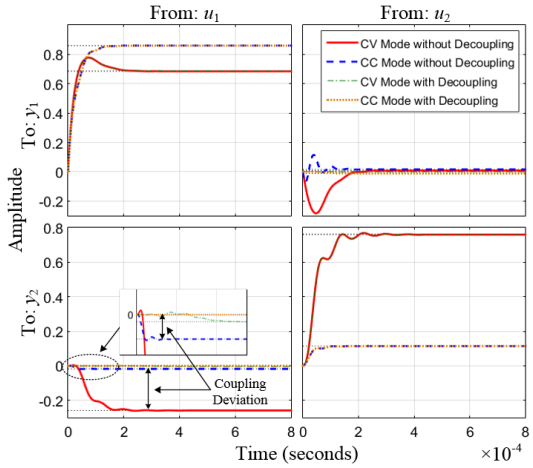

FIGURE 3. Unit step responses of the linearized MIMO CC/CV models with/without the decoupled compensators.

matrix method, the compensation matrices $W_{\mathrm{d}}(s)$ can be calculated per

$$W_{\mathrm{d}}(s) = G(s)^{-1} N_{\mathrm{L}}(s), \tag{27}$$

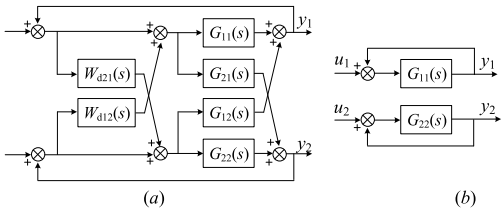

FIGURE 4. The block diagram of the (a) decoupled compensator and (b) decoupled system.

where $G(s)$ is the transfer function models of the CC and CV modes, and $N_{\mathrm{L}}(s)$ is the diagonal elements of $G(s)$. Due to the high order of $W_{\mathrm{d}}(s)$, the balanced truncation method [36] is used to reduce the order of the compensators. Hence, the compensation transfer functions from u_1 to y_2, and from u_2 to y_1 for the CC and CV linearized models can be obtained as

$$W_{\mathrm{dcc21}}(s) = \frac{-1163s + 1.2e10}{s^2 + 2.8e4s + 1.3e10},$$
$$W_{\mathrm{dcc12}}(s) = \frac{-1163s + 1.2e10}{s^2 + 2.8e4s + 1.3e10} \tag{28}$$
$$W_{\mathrm{dcv21}}(s) = \frac{-7.1s^2 + 6.7e9 + 1.3e14}{s^3 + 4.6e4s^2 + 3e9s + 2.4e13}$$
$$W_{\mathrm{dcv12}}(s) = \frac{-7.1s^2 + 6.7e9 + 1.3e14}{s^3 + 4.6e4s^2 + 3e9s + 2.4e13}. \tag{29}$$

The unit step responses of the CC and CV linearized models with the decoupled compensations are plotted in Fig. 3. Compared to the curves without the compensators, one can see that the fluctuations and the static deviation are suppressed and compensated to zero. Therefore, the multivariable models are simplified to two single variable models with the diagonal elements of $G(s)$ as shown in Fig. 4(b).

B. DESIGN OF THE EV CHARGING AND ZVS OPERATING LOOP CONTROLLERS

The diagonal transfer function models $N_{\mathrm{L}}(s)$ of the CC and CV linearized models are

$$\begin{aligned} &N_{\mathrm{LCC11}}(s) \\ &= \frac{3.6e4s^3 + 2.7e9s^2 + 3.7e14s + 1e19}{s^4 + 1.2e5s^3 + 1.5e10s^2 + 8e14s + 1.3e19} \\ &N_{\mathrm{LCC22}}(s) \\ &= \frac{1315s^3 1.5e8s^2 + 4.6e13s + 1.5e18}{s^4 + 1.2e5s^3 + 1.5e10s^2 + 8.1e14s + 1.3e19} \\ &N_{\mathrm{LCV11}}(s) \\ &= \frac{3.6e4s^4 + 5e9s^3 + 4e14s^2 + 3e19s + 4e23}{s^5 + 2e5s^4 + 1.6e10s^3 + 1e15s^2 + 4e19s + 5.5e23} \\ &N_{\mathrm{LCV22}}(s) \\ &= \frac{1.8e8s^3 + 9.5e13s^2 + 1e19s + 4.2e23}{s^5 + 2e5s^4 + 1.6e10s^3 + 1e15s^2 + 4e19s + 5.5e23}, \end{aligned} \tag{30}$$

where $N_{\mathrm{LCC11}}(s)$ and $N_{\mathrm{LCC22}}(s)$ are the transfer functions of the CC charging mode from u_1 to y_1, and from u_2 to y_2, respectively; $N_{\mathrm{LCV11}}(s)$ and $N_{\mathrm{LCV22}}(s)$ are the transfer functions of the CV charging mode from u_1 to y_1, and from u_2 to y_2, respectively. The unity feedback root locus of (30) is plotted in Fig. 5. By analyzing the distribution of the closed-loop zero-pole, the following conclusion can be obtained:

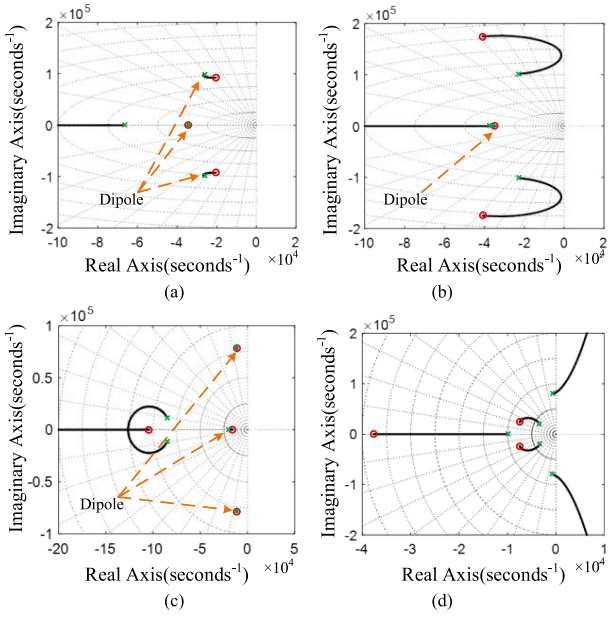

FIGURE 5. Unity feedback root locus of (a) $N_{\mathrm{LCC11}}(s)$, (b) $N_{\mathrm{LCC22}}(s)$, (c) $N_{\mathrm{LCV11}}(s)$ and (d) $N_{\mathrm{LCV22}}(s)$.

(1) The stability of (30) is available because the closed-loop poles are all located in the left s-plane. However, the plural poles of $N_{\mathrm{LCV22}}(s)$, as depicted in Fig. 5 (d), indicate that the stability of the charging voltage in the CV mode is conditional.

(2) Since the dynamic performance of the model mainly depends on the real part and attenuation rate of the dominant pole, a dipole can be ignored if the distance between its zero and pole is much smaller than its distance from the origin.

(3) The proportion and integration elements of the PI controllers in each control-loop are equivalent to add a new closed-loop zero and a new dominant pole to the models. Therefore, the parameters of the controllers can be calculated by arranging the distribution of the closed-loop dominant pole with reference to the performance requirements of the settling time and overshoot.

The PI controller has the following form:

$$G_c(s) = K_p\left(1 + \frac{1}{T_i s}\right), \tag{31}$$

where K_p and T_i are the proportional coefficient and the integral time, respectively. According to the decoupled system, as shown in Fig. 4 (b), the closed-loop transfer function with the PI controller of each control-loop can be expressed as

$$\Phi(s) = \frac{G_c(s)N_L(s)}{G_c(s)N_L(s) + 1} \approx \frac{\omega_n^2}{z}\frac{(s+z)}{s^2 + 2\xi\omega_n + \omega_n^2}, \tag{32}$$

where ω_{n} and ξ are the natural frequency and damping ratio of the closed-loop dominant pole brought by the PI controllers. Thus, the closed-loop characteristic equation of (32) is

$$s^2 + 2\xi\omega_n + \omega_n^2 \approx K_p(s + K_i)\prod_{i=1}^{m}(s - z_i) + 1 = 0, \tag{33}$$

Assuming that the performance requirements of the settling time and overshoot are $t_{\mathrm{s}} = 200$ ms and $\sigma\% = 5\%$ with an error band of 5%, the distribution of the dominant pole can be calculated by

$$\begin{aligned} t_s &= 3.5/\xi\omega_n \\ \sigma\% &= e^{-\pi\xi/\sqrt{1-\xi^2}} \times 100\%. \end{aligned} \tag{34}$$

Using MATLAB, the final parameters of the CC and CV PI controllers are calculated as: $K_{p\mathrm{CC}} = 0.8$, $T_{i\mathrm{CC}} = 0.003$; $K_{p\mathrm{CCZVS}} = 0.1$, $T_{i\mathrm{CCZVS}} = 0.03$; $K_{p\mathrm{CV}} = 0.1$, $T_{i\mathrm{CV}} = 0.003$; $K_{p\mathrm{CVZVS}} = 0.15$, $T_{i\mathrm{CVZVS}} = 0.026$.

V. EXPERIMENTAL RESULTS

A. THE WCS PROTOTYPE

Fig. 6 shows the physical experimental setup in terms of the topology circuit in Fig. 1. The experimental setup consists of a controllable DC source, a PCB including a half-bridge inverter, MCUs and a wireless communication module, an S-S resonant network, a full-bridge rectifier and four switchable power resistors. The parameters of the components are shown in Table 1. Two IPW65R041CFD MOSFETs are used for the half-bridge inverter, and the controllers are implemented with two MCUs, namely, an FPGA (XC6SLX9-3TQG144I) and an ARM (STM32F407VGT). The type of the controllable DC source is INFY POWER REG75030, and it is given in the data sheets that the control interval

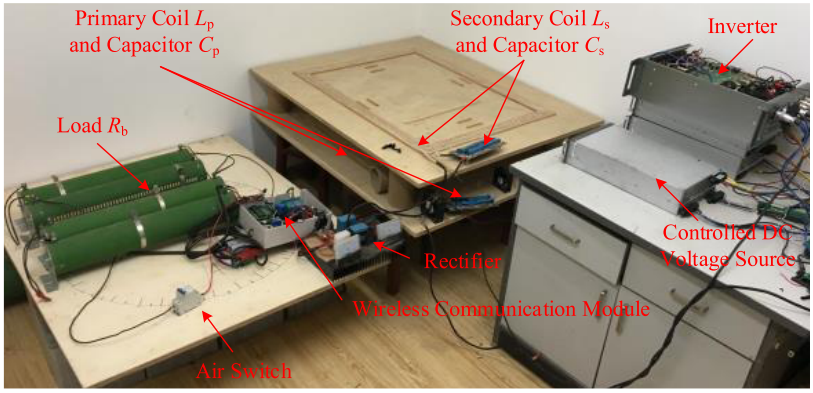

FIGURE 6. Physical experimental setup of the S-S compensated wireless charging system.

and the settling time of the output voltage are about 40 ms and 6 ms, respectively. The range of the output voltage is listed in Table 1. The ARM is used to calculate the operating frequency and input DC voltage of the inverter, while the FPGA and DC source regulate the inverter driving signals and input DC voltage with a control period of 40 ms and 20 ms, respectively, according to the ZVS angle and charging commands from the ARM. The wireless communication for the charging current and voltage data are set up with two nRF24L01 modules. The dimensions of the two coaxial coils are the same, whose rectangular outer ring is 90 cm $\times$ 70 cm. The distance between the coils is 20 cm. Each coil is built with four turns of Liz-wire. The diameter of the Litz-wire consisting of 2000 isolated strands is 6 mm, and the diameter of each strand is 0.1 mm. At the secondary side, a class-D full-bridge rectifier is constructed using four VS-UFB280FA40 diodes. For the load, different resistance values are obtained by connecting four 10 Ω resistors in series or in parallel with an air switch.

B. EXPERIMENT OF CC AND CV CHARGING

To validate the improvement of the control performance of the system with the proposed decoupled control method, three cases of experiments are set up in this paper, namely, (i) decoupled control, (ii) coupled control, and (iii) traditional closed-loop feedback control. According to the range of the ESR of the lead battery during the charging process [5]–[7], two step changes of the load resistance for the CC and CV charging modes, namely, from 2.5 Ω to 5 Ω and from 7.5 Ω to 10 Ω, respectively, are considered as the disturbances in the experiment.

By step change of the resistor bank, the dynamic responses of the charging current and voltage in case (i) are captured by an oscilloscope (Tektronix DPO 2004B) as shown in Fig. 7(a) and (b). It can be seen that both the charging current and the voltage can reach the constant references, namely, 10 A and 50 V, within 200 ms which are in good agreement with the preset performance requirements. In addition, the dynamic waveforms for case (ii) and case (iii) in each charging mode are depicted in Fig. 7(c), (d), (e) and (f), respectively. In case (ii), when the load changes, the settling times of the CC and CV modes are all 235 ms. Meanwhile, the charging current and voltage in case (iii) can reach the reference within 435 ms and 420ms, respectively. What is worth mentioning, comparing with the case (i), the settling times of the case (ii) and case (iii) are longer than the requirements. In addition, the same tendency can also be observed in the overshoots. Therefore, the following conclusions can be obtained:

(1) The charging current and voltage in both CC and CV modes can reach the reference with the above control methods, namely, cases (i)-(iii).
(2) The proposed decoupled control method (case (i)) can obtain a better control performance than other control methods. This is because that the couplings between the charging loop and the ZVS operation loop are accurately calculated in the solving process of the compensation transfer functions, therefore, the compensators can eliminate the fluctuations and improve the control performance. In contrast, the controllers for case (ii) and (iii) need more time to deal with the couplings of the system and the change of the operation point.
(3) In Fig. 7 (c) and (d), although the charging current and voltage need more time to return to the reference compared to case (i), they response faster than that in case (iii). This proves that the PI controllers which designed on the basis of the corresponding models are more robust to the change of the operating point.

For ZVS operation control, the phase difference between the output voltage and current of the inverter is measured by the FPGA and current sensor. In this paper, the data of the ZVS angle is calculated and saved by the MCUs and RS232 communication circuit at a period of 20 ms. Therefore, the waveforms of the ZVS angles in the CC and CV charging modes with different control methods (case (i)-(iii)) are plotted in Fig. 8 (a) and (b). Although the ZVS angles rise rapidly when the load changes, they gradually return to the reference of 20°, and no overshoots are observed in

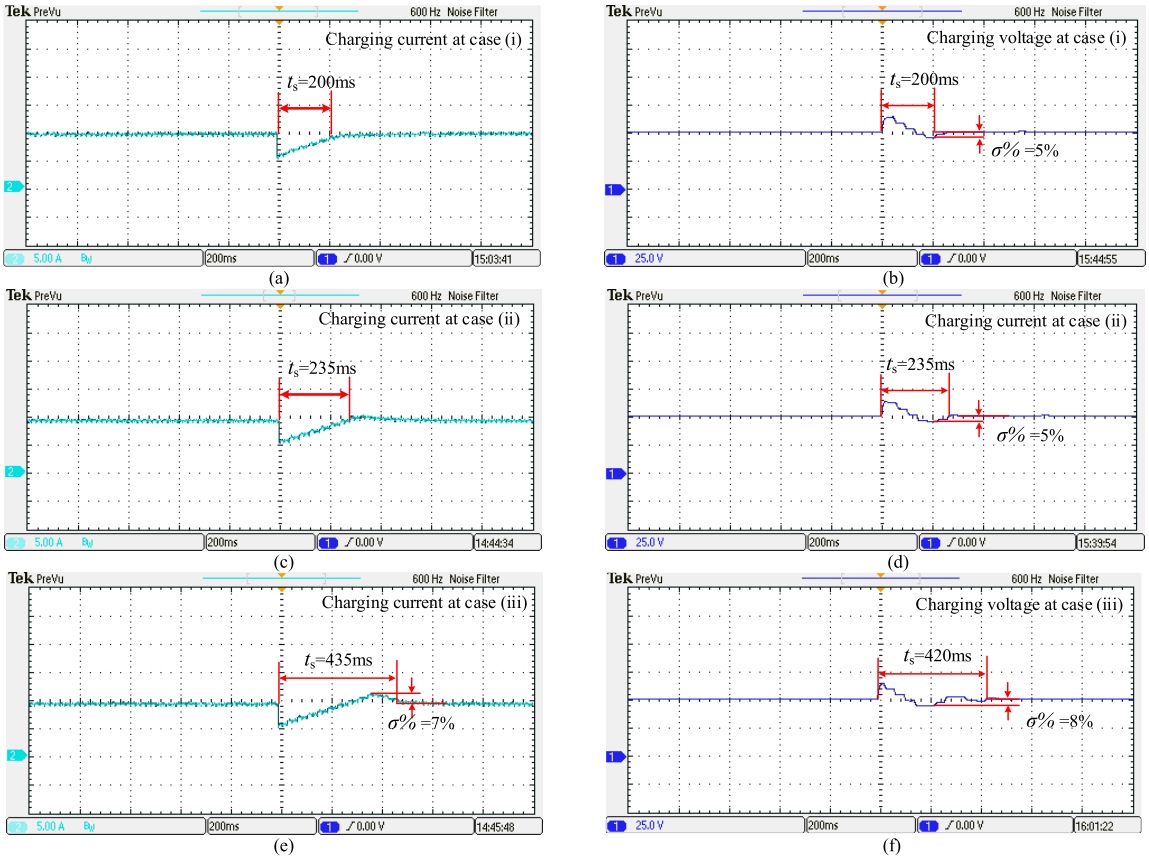

FIGURE 7. The Dynamic waveforms of the charging current and voltage when the load resistance changes. (a) and (b) are the charging current and voltage in the case (i); (b) and (c) are the charging current and voltage in the case (ii); (e) and (f) are the charging current and voltage in the case (iii).

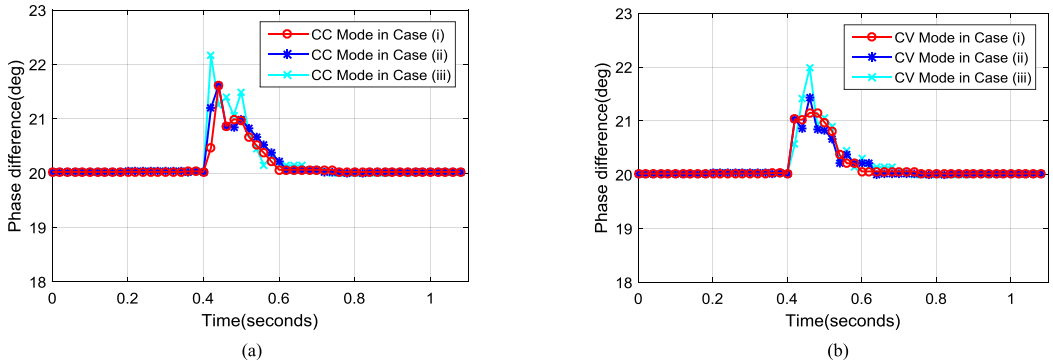

FIGURE 8. Dynamic waveforms of the ZVS angle in the (a) CC and (b) CV charging modes when the load resistance changes.

each case. Similar to the charging control-loop, the ZVS angles of the CC and CV modes in case (i) can obtain a better control performance, and reach the steady-state within 200 ms.

Since the system is semi-coupled, compared with the waveforms in Fig. 7, the proposed decoupled compensator has less improvement to the performance of the ZVS operation. In addition, since the dynamic fluctuation in the CV mode is larger than that in the CC mode, as depicted in Fig. 3, the decoupled compensator plays a more significant role in the CV charging mode. Furthermore, it can be seen that the settling times of the case (ii) are shorter than the case (iii), which also proves that the PI controllers based on different dynamic models can prevent the degradation of the performance caused by the change of the operating point.

The steady-state waveforms of the inverter output voltage and current in the CC and CV modes are captured by an oscilloscope and shown in Fig. 9 (a) through (d). One can see from Fig. 9 (a) that the ZVS angle and operating frequency in the CC mode are about 20° and 84.91 kHz, respectively. When the load resistance step rises to 5 Ω, as shown in Fig. 9 (b), the steady-state ZVS angle can be maintained at

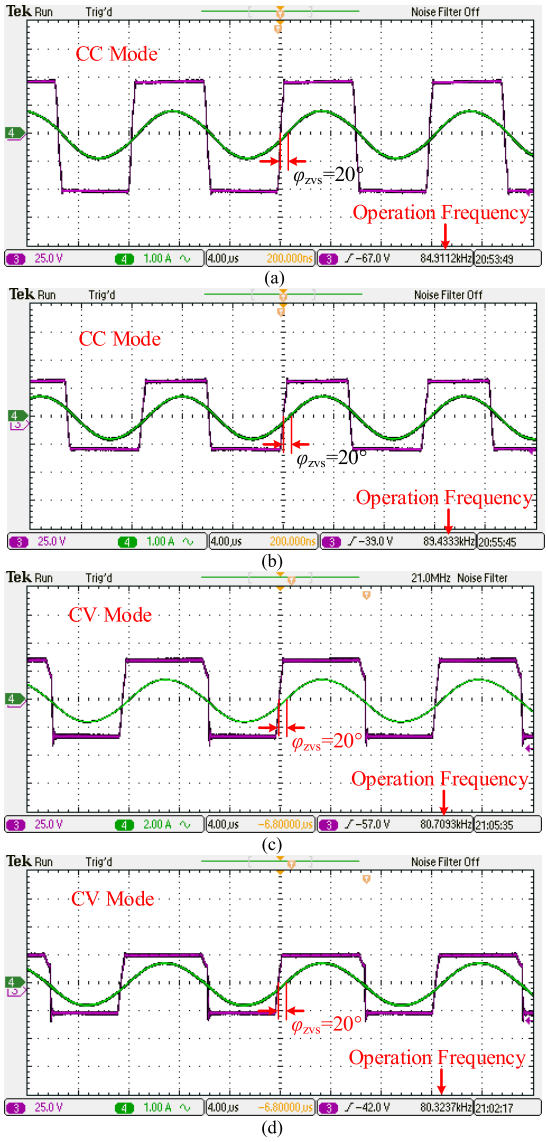

FIGURE 9. Steady-state waveforms of the output voltage and current of the inverter with the decoupled control method. (a) and (b) are the waveforms in the CC charging mode when the load resistance changes from 2.5 Ω to 5 Ω; (c) and (d) are the waveforms in the CV charging mode when the load resistance changes from 7.5 Ω to 10 Ω.

the reference of 20°, and the operating frequency is adjusted to 89.43 kHz. The same tendency can be observed in CV mode in Fig. 9 (c) and (d). When a disturbance is given to change the load resistance from 7.5 Ω to 10 Ω, the operating frequency is regulated from 80.71 kHz to 80.32 kHz to maintain the ZVS angle at constant. The above two sets of waveforms all illustrate that the ZVS operation can be achieved by changing the operating frequency of the inverter.

VI. CONCLUSION

In this paper, we propose a decoupled control method to improve the performance of the charging and ZVS operation controllers in the WCS. Since the operating point of the CC and CV modes are different, two dynamic models for the corresponding modes are built and linearized. By analyzing the couplings and distributions of the zero-pole, the decoupled compensators are designed to neutralize the deviations and fluctuations. Meanwhile, to optimize the system performance, we chose PI controllers, and their parameters are obtained by calculating the settling time and overshoot of the close-loop dominant poles according to the requirements of the control performance, which is especially useful when the control system is required to be designed tightly. To verify the improvement of the performance with the decoupled control method, a 500W S-S inductive power transfer system prototype is built and tested. The recorded response curves and steady-state waveforms demonstrated that the charging current, voltage and ZVS angle can reach the references in the whole charging period. Furthermore, the proposed decoupled controllers can achieve a better control performance compared with the coupled control method and the traditional closed-loop feedback control method.

APPENDIX

$$K_1 = \frac{\sqrt{L_p/2}}{L_p L_s - M^2}$$
$$K_2 = \frac{\sqrt{L_s/2}}{L_p L_s - M^2}$$
$$K_3 = \frac{M}{\sqrt{2C_s}}$$
$$K_4 = \frac{M}{\sqrt{2C_p}}$$
$$K_5 = \frac{(R_s + R_{cd})}{\sqrt{2L_s}}$$
$$K_6 = \frac{MR_p}{\sqrt{2L_p}}$$
$$K_7 = \frac{L_s}{\sqrt{2C_p}}$$
$$K_8 = \frac{L_p}{\sqrt{2C_s}}$$
$$S_1 = \sin(x_2 - x_4)$$
$$S_2 = \cos(x_2 - x_4)$$

REFERENCES

[1] Q. Deng, J. Liu, D. Czarkowski, W. Hu, and H. Zhou, "An inductive power transfer system supplied by a multiphase parallel inverter," *IEEE Trans. Ind. Electron.*, vol. 64, no. 9, pp. 7039–7048, Mar. 2017.

[2] Q. Deng *et al.*, "Frequency-dependent resistance of Litz-wire square solenoid coils and quality factor optimization for wireless power transfer," *IEEE Trans. Ind. Electron.*, vol. 63, no. 5, pp. 2825–2837, May 2016.

[3] J. Liu, Q. Deng, D. Czarkowski, M. K. Kazimierczuk, H. Zhou, W. Hu, "Frequency optimization for inductive power transfer based on AC resistance evaluation of Litz-wire," *IEEE Trans. Power Electron.*, to be published, doi: 10.1109/TPEL.2018.2839626.

[4] G. Buja, M. Bertoluzzo, and K. N. Mude, "Design and experimentation of WPT charger for electric city car," *IEEE Trans. Ind. Electron.*, vol. 62, no. 12, pp. 7436–7447, Dec. 2015.

[5] Q. Deng, J. Liu, D. Czarkowski, M. Bojarski, E. Asa, and F. de Leon, "Design of a wireless charging system with a phase-controlled inverter under varying parameters," *IET Power Electron.*, vol. 9, no. 13, pp. 2461–2470, Oct. 2013.

[6] A. Khaligh and Z. Li, "Battery, ultracapacitor, fuel cell, and hybrid energy storage systems for electric, hybrid electric, fuel cell, and plug-in hybrid electric vehicles: State of the art," *IEEE Trans. Veh. Technol.*, vol. 59, no. 6, pp. 2806–2814, Jul. 2010.

[7] Y. Jiang, L. Wang, Y. Wang, J. Liu, X. Li, and G. Ning, "Analysis, design and implementation of accurate ZVS angle control for EV's battery charging in wireless high power transfer," *IEEE Trans. Ind. Electron.*, to be published, doi: 10.1109/TIE.2018.2795523.

[8] J. Tian and A. P. Hu, "A DC-voltage-controlled variable capacitor for stabilizing the ZVS frequency of a resonant converter for wireless power transfer," *IEEE Trans. Power Electron.*, vol. 32, no. 3, pp. 2312–2318, Mar. 2016.

[9] Q. Chen, S. C. Wong, C. K. Tse, and X. Ruan, "Analysis, design, and control of a transcutaneous power regulator for artificial hearts," *IEEE Trans. Biomed. Circuits Syst.*, vol. 3, no. 1, pp. 23–31, Feb. 2009.

[10] P. Tan, H. He, and X. Gao, "A frequency-tracking method based on a SOGI-PLL for wireless power transfer systems to assure operation in the resonant state," *J. Power Electron.*, vol. 16, no. 3, pp. 1056–1066, May 2016.

[11] J. Shin *et al.*, "Design and implementation of shaped magnetic-resonance-based wireless power transfer system for roadway-powered moving electric vehicle," *IEEE Trans. Ind. Electron.*, vol. 61, no. 3, pp. 1179–1192, Mar. 2014.

[12] B. Wang, A. P. Hu, and D. Budgett, "Maintaining middle zero voltage switching operation of parallel-parallel tuned wireless power transfer system under bifurcation," *IET Power Electron.*, vol. 7, no. 7, pp. 78–84, Jan. 2014.

[13] W. Shi, J. Deng, Z. Wang, and X. Cheng, "The start-up dynamic analysis and one cycle control-PD control combined strategy for primary-side controlled wireless power transfer system," *IEEE Access*, vol. 6, pp. 14439–14450, Mar. 2018.

[14] R. Mai, L. Ma, Y. Liu, P. Yue, G. Cao, and Z. He, "A maximum efficiency point tracking control scheme based on different cross coupling of dual-receiver inductive power transfer system," *Energies*, vol. 10, no. 5, p. 217, Feb. 2017.

[15] X. Lu, J. Lai, X. Yu, Y. Wang, and J. M. Guerrero, "Distributed coordination of islanded microgrid clusters using a two-layer intermittent communication network," *IEEE Trans. Ind. Informat.*, vol. 14, no. 9, pp. 3956–3969, Sep. 2018, doi: 10.1109/TII.2017.2783334.

[16] H. Li, J. Li, K. Wang, W. Chen, and X. Yang, "A maximum efficiency point tracking control scheme for wireless power transfer systems using magnetic resonant coupling," *IEEE Trans. Power Electron.*, vol. 30, no. 7, pp. 3998–4008, Jul. 2015.

[17] J. Lai, H. Zhou, X. Lu, X. Yu, and W. Hu, "Droop-based distributed cooperative control for microgrids with time-varying delays," *IEEE Trans. Smart Grid*, vol. 7, no. 4, pp. 1775–1789, Jul. 2016.

[18] F. Pijl, M. Castilla, and P. Bauer, "Adaptive slide-mode control for a multiple-user inductive power transfer system without need for communication," *IEEE Trans. Ind. Electron.*, vol. 60, no. 1, pp. 271–279, Jan. 2013.

[19] X. Yin, Y.-G. Lin, W. Li, Y.-J. Gu, P.-F. Lei, and H.-W. Liu, "Sliding mode voltage control strategy for capturing maximum wind energy based on fuzzy logic control," *Int. J. Elect. Power Energy Syst.*, vol. 70, pp. 45–51, Sep. 2015.

[20] A. K. Swain, M. J. Neath, U. K. Madawala, and D. J. Thrimawithana, "A dynamic multivariable state-space model for bidirectional inductive power transfer systems," *IEEE Trans. Power Electron.*, vol. 27, no. 11, pp. 4772–4780, Nov. 2012.

[21] C. Zheng *et al.*, "High-efficiency contactless power transfer system for electric vehicle battery charging application," *IEEE J. Emerg. Sel. Topics Power Electron.*, vol. 3, no. 1, pp. 65–74, Mar. 2015.

[22] V.-B. Vu, D.-H. Tran, and W. Choi, "Implementation of the constant current and constant voltage charge of inductive power transfer systems with the double-sidedlcccompensation topology for electric vehicle battery charge applications," *IEEE Trans. Power Electron.*, vol. 33, no. 9, pp. 7398–7410, Sep. 2018, doi: 10.1109/TPEL.2017.2766605.

[23] S. Lee, B. Choi, and C. T. Rim, "Dynamics characterization of the inductive power transfer system for online electric vehicles by Laplace Phasor transform," *IEEE Trans. Power Electron.*, vol. 28, no. 12, pp. 5902–5909, Dec. 2013.

[24] J. Huh, W. Lee, G.-H. Cho, B.-H. Lee, and C.-T. Rim, "Characterization of novel inductive power transfer systems for on-line electric vehicles," in *Proc. IEEE Appl. Power Electron. Conf. Expo.*, Mar. 2011, pp. 1975–1979.

[25] H. Hao, G. A. Covic, and J. T. Boys, "An approximate dynamic model of LCL-T-based inductive power transfer power supplies," *IEEE Trans. Power Electron.*, vol. 29, no. 10, pp. 5554–5567, Oct. 2014.

[26] W. Li, H. Zhao, S. Li, J. Deng, T. Kan, and C. C. Mi, "Integrated LCC compensation topology for wireless charger in electric and plug-in electric vehicles," *IEEE Trans. Ind. Electron.*, vol. 62, no. 7, pp. 4215–4225, Jul. 2015.

[27] Z. Huang, S.-C. Wong, and C. K. Tse, "Control design for optimizing efficiency in inductive power transfer systems," *IEEE Trans. Power Electron.*, vol. 33, no. 5, pp. 4523–4534, May 2017.

[28] R. Tavakoli and Z. Pantic, "Analysis, design, and demonstration of a 25-kW dynamic wireless charging system for roadway electric vehicles," *IEEE J. Emerg. Sel. Topics Power Electron.*, vol. 6, no. 3, pp. 1378–1393, Sep. 2018, doi: 10.1109/JESTPE.2017.2761763.

[29] Z. U. Zahid *et al.*, "Modeling and control of series–series compensated inductive power transfer system," *IEEE J. Emerg. Sel. Topics Power Electron.*, vol. 3, no. 1, pp. 111–123, Mar. 2015.

[30] M. M. Rana, W. Xiang, E. Wang, X. Li, and B. J. Choi, "Internet of Things infrastructure for wireless power transfer systems," *IEEE Access*, vol. 6, pp. 19295–19303, Jan. 2018.

[31] Y. Li, J. Hu, F. Chen, Z. Li, Z. He, and R. Mai, "Dual-phase-shift control scheme with current-stress and efficiency optimization for wireless power transfer systems," *IEEE Trans. Circuits Syst. I, Reg. Papers*, vol. 65, no. 9, pp. 3110–3121, Apr. 2018.

[32] H. Li, K. Wang, L. Huang, W. Chen, and X. Yang, "Dynamic modeling based on coupled modes for wireless power transfer systems," *IEEE Trans. Power Electron.*, vol. 30, no. 11, pp. 6245–6253, Nov. 2015.

[33] H. Li, J. Li, L. Huang, K. Wang, and X. Yang, "A novel dynamic modeling method for wireless power transfer systems," in *Proc. IEEE Appl. Power Electron. Conf. Expo.*, Mar. 2015, pp. 2740–2743.

[34] A. Kurs, A. Karalis, R. Moffatt, J. D. Joannopoulos, P. Fisher, and M. Soljačić, "Wireless power transfer via strongly coupled magnetic resonances," *Science*, vol. 317, no. 5834, pp. 83–86, 2007.

[35] M. K. Kazimierczuk and D. Czarkowski, "Class D current-driven rectifiers," in *Resonant Power Converters*, 2nd ed. Hoboken, NJ, USA: Wiley, 2011, pp. 60–63.

[36] S. Zheng and D. Czarkowski, "Modeling and digital control of a phase-controlled series-parallel resonant converter," *IEEE Trans. Ind. Electron.*, vol. 54, no. 2, pp. 707–715, May 2007.

CHENG CHEN (S'18) received the B.S. degree in mechanical engineering from the Wuhan Institute of Bioengineering, Wuhan, China, in 2012, and the M.S. degree in control engineering from Wuhan University, Wuhan, in 2015, where he is currently pursuing the Ph.D. degree with the School of Power and Mechanical Engineering. His current research interests include system modeling, nonlinear control, and wireless power transfer.

HONG ZHOU (M'18) received the B.S. degree from the Central South University of Technology (now Central South University), Changsha, China, in 1982, the M.Sc. degree from Chongqing University, Chongqing, China, in 1988, and the Ph.D. degree from Wuhan University, Wuhan, China, in 2006.

He was an Assistant Engineer with Changshou Power Plant, Chongqing, from 1982 to 1985. He has been with the Wuhan University of Hydraulic and Electrical Engineering (now a part of Wuhan University), Wuhan, since 1992. He was the Head of the Department of Automation, Wuhan University, from 2002 to 2006, where he has been a Professor since 2000. His main research interests are wireless power transfer, smart grid, and networked control systems.

QIJUN DENG received the B.S. and M.Sc. degrees in mechanical engineering and the Ph.D. degree in computer application technology from Wuhan University, Wuhan, China, in 1999, 2002, and 2005, respectively.

In 2005, he joined the Department of Automation, Wuhan University, where he is currently an Associate Professor. From 2013 to 2014, he was a Visiting Scholar with the New York University Tandon School of Engineering. His research interests include wireless power transfer, distribution automation, and electrical power informatics.

WENSHAN HU (M'18) received the B.S. and M.Sc. degrees in control theory and applications from Wuhan University, Wuhan, China, in 2002 and 2004, respectively, and the Ph.D. degree in control engineering from the University of Glamorgan, Pontypridd, U.K., in 2008. He is currently a Professor with the Department of Automation, Wuhan University. His research interests include wireless power transfer and network-based control laboratories.

YANJUAN YU received the B.S. degree in control theory and applications from Wuhan University, Wuhan, China, in 2013, where she is currently pursuing the Ph.D. degree with the School of Electrical Engineering.

Her research interests include wireless power transfer, mathematical optimization, renewable energy accommodation, and integrated energy system.

XIAOQING LU received the Ph.D. degree in applied mathematics from Wuhan University, Wuhan, China, in 2012. She is currently a Professor with the Department of Automation, School of Power and Mechanical Engineering, Wuhan University. She is also a Post-Doctoral Research Fellow with the School of Engineering, RMIT University, Melbourne, Australia. Her research interests include nonlinear dynamical systems, intelligent systems and applications, complex networks, multiagent systems, and microgrids.

JINGANG LAI (M'17) received the Ph.D. degree in control science and engineering from Wuhan University, Wuhan, in 2016. He was a Joint Ph.D. Student with the School of Electrical and Computer Engineering, RMIT University, Melbourne, VIC, Australia, in 2015.

He is currently a Research Fellow with the School of Engineering, RMIT University. His research interests include smart grid, microgrid control, and networked control systems.